ABOUT FLAME - ACOUSTIC COUPLING PHENOMENA IN SUPERCRITICAL H_2/O_2 ROCKET COMBUSTION SYSTEMS

Dipl.-Ing. M. Schulze, M. Zahn (M.Sc.), Dipl.-Ing. M. Schmid
and Prof. Dr.-Ing. T. Sattelmayer

Technische Universität München, Lehrstuhl für Thermodynamik, Boltzmannstr. 15,
Garching b. München, D-85747

Abstract

The dynamic flame response to acoustic excitation is numerically analyzed for a typical rocket engine application with supercritical H_2/O_2 combustion in a coaxial injector configuration. To reduce numerical efforts the frame of consideration is restricted to only a single flame, leading to low computational times and to the possibility of applying fast turnaround times. In each simulation, the single flame is subjected to an artificially generated acoustic field for a single-frequency excitation and is studied in terms of fluctuating heat release rates and governing periodic field structures. Parameter studies are carried out to analyze the coupling mechanisms, which are responsible for the fluctuating nature of the heat release rate. Studies show that the flame response depends on excitation frequency, which is varied between 8 000 and 16 000 Hz, and load point. Further investigations show that two different coupling mechanisms are present in the chamber which can be spatially distinguished. In the region close to the injector, the convective transport of periodically oscillating vortices is dominant. In the remaining region further downstream baroclinic effects due to strong density gradients in combination with axial acoustic pressure gradients govern the the periodic generation of vortices, which, in turn, lead to a fluctuating heat release rate. Those two mechanism provide unequal contributions to the total fluctuating heat release rate, providing different driving potentials for thermoacoustic instability.

NOMENCLATURE

x, r, φ	.....	cylindrical coordinates [m]
t	.....	time [s]
i	.....	imaginary unit
p	.....	pressure [Pa]
v_i	.....	velocity $[m/s]$
v	.....	molar volume $[m^3/mol]$
$\bar{\rho}$	.....	mean density $[\mathrm{kg/m^3}]$
c	.....	speed of sound [m/s]
$\hat{g}$	.....	Riemann Invariant, upstream direct. [m/s]
J_1	.....	Bessel function of first kind and order one
s_{10}	.....	1.8412, 0-th root of $d\mathrm{J}_1(x)/dx$
d_{cc}	.....	combustion chamber diameter [m]
ω	.....	angular frequency [rad/s]
f	.....	frequency $[1/s]$
R_{FP}	.....	reflection coefficient at the face plate
$k, k^{\pm}$	.....	wave numbers $[1/\mathrm{m}]$
M	.....	Mach number
f_{cut}	.....	cut-on frequency $[1/s]$
$\overline{\dot{\omega}_{\mathrm{H_2}}}$	.....	fuel mean burning rate $[1/s]$
A, B	.....	model constants, see [1]
$Y_{\mathrm{H_2/O_2/H_2O}}$	.....	mass fraction $(\mathrm{H_2}, \mathrm{O_2}, \mathrm{H_2O})$
$\nu'_{\mathrm{O_2}}, \nu'_{\mathrm{H_2}}$	.....	stoichiometric coefficients
$W_{\mathrm{O_2/H_2}}$	.....	atomic weight [kg/kmol]
$\blacksquare'$	.....	fluctuating quantity
$\hat{\blacksquare}$	.....	complex amplitude
$\widetilde{\blacksquare}$	.....	averaging operator
$\blacksquare_c$	.....	quantity at critical point

1. INTRODUCTION

For the judgement of thermoacoustic feedback phenomena in confined combustion systems, so-called combustion instabilities, the understanding of the flame dynamics under acoustic influence is crucial. On the one hand, potential danger of unstable configurations can be examined on the basis of known coupling mechanisms. On the other hand, design modifications can be derived and implemented to prevent the occurance of dangerous pressure and temperature amplitudes. It has been shown in the past that a wide variety of measures, e.g. design changes of the injection sytem or even the substitution of the propellants can contribute to limit acoustic amplitudes to tolerable levels.

Nowadays computer aided design procedures demand for high quality numerical prediction tools of thermoacoustic stability. The development of such methods is, however, still an unfulfilled task [2]. Considering especially the trend towards alternative fuels such as methane [3], reliable predictions are of essential importance since the wealth of experience is less than for conventional propellants like hydrogen/oxygen. At the same time these methods are supposed to be lean in terms of computational times and effort.

Against this background, a CFD/CAA approach has been developed at the Lehrstuhl für Thermodynamik, Technische Universität München, see [4,5,6,7]. The essential ingredient to reduce computational effort is to exploit separation of small scale effects such as turbulent combustion from considerable bigger scales of acoustic propagation. Different numerical environments to establish

the most suitable techniques to solve for the different scales are applied. Consequently high quality results can be achieved in each computation including all relevant effects. The links between the computations are described in form of transfer functions, which include the essential mechanisms for thermoacoustic phenomena. For example the dynamic flame response under acoustic influence, i.e. the driver for thermoacoustic feedback, is calibrated in form of flame transfer functions and incorporated into the stability prediction as a volumetric energy source term to close the feedback loop.
The generation of flame transfer functions for a rocket engine configuration, including hundreds of injectors, in a numerical environment is out of reach for state of the art methods. Meaningful results can, however, be achieved through a reduction of the frame of consideration to only a single flame. Not only can single flame considerations be used to calibrate flame transfer functions, but also fundamental studies on the relevant coupling mechanisms between acoustics and combustion can be conducted. Such knowledge is essential to develop adequate designs in order to suppress the occurrence of combustion instabilities right from the beginning of the development cycle or to take appropriate measures for existing designs, which suffer from high thermoacoustic loads.
In this paper a method to excite a single flame configuration according to [8,9,10] is presented and applied to a supercritical combustion system. As test case DLR's BKD test chamber is used. Different frequencies and load points are considered. On the basis of recorded signals of pressure and heat release rate as well as of dynamic mode decomposition (DMD) results, physical understanding of the governing coupling processes is gained and their relevance for thermoacoustic feedback is addressed. Finally, flame transfer functions for two load points are derived and used to conclude their driving potential for thermoacoustic instability.
The structure of this paper reads as follows. Section 2 explains the main modeling aspects including the single injector excitation method, turbulence and combustion modeling as well as real gas relations. Section 3 introduces the test case. Afterwards, section 4 presents the results in terms of dynamic flame response and explains possible underlying coupling mechanisms. In section 5, the achievements of the presented work are discussed and an outlook of future goals is given.

2. MODELLING ASPECTS

The modelling of combustion in rocket engines is challenging due to high pressure conditions and a wide temperature range. A large number of injectors in a highly turbulent and reacting environment have to be considered. To benefit from low storage temperatures cryogenically driven engines are often used. In such systems, ideal gas relations are not valid in the region of propellant injection. Essentially, for a meaningful calculation of the momentum of propellants in that region, intermolecular forces have to be included, and an accurate prediction of the flame length can then be expected.
In the following the excitation method is presented together with the applied turbulence and combustion modelling. Real-gas relations for an adequate treatment of thermodynamics are explained afterwards. Finally the numerical setup is outlined.

2.1. Single injector excitation method

In the computational analysis of [4] and within the experiments of [11,12], the first transverse acoustic mode was determined as the most critical for rocket engine applications. According to [13] this is due to high damping capabilities of the thrust nozzle for longitudinal modes. Transverse modes, in turn, are only weakly attenuated and remain as most acoustic energy containing structures in the combustion chamber.
Based on the acoustic pressure field of the first transverse mode in the combustion chamber, an acoustic excitation method has been developed by [8,9,10], in which only one flame configuration with periodic boundaries is considered to save computational cost. Essentially, its derivation is based on the assumption of acoustic compactness in transverse direction, which becomes more and more meaningful with an increasing total number of injectors and therefore reduced single injector diameters, see Fig. 1. In axial direction, however, a significant pressure amplitude distribution due to convective effects, heat release and accompanied temperature gradients, frequency effects as well as influences of stratification and the thrust nozzle is present.
In general, the flame response to pressure fluctuations and to transverse velocity fluctuations is different. The response to pressure fluctuations can be studied by considering a single flame configuration located in the pressure anti-node, whereas a flame configuration located in the velocity anti-node is subjected to velocity fluctuations exclusively. The dynamics of the remaining flame configurations are determined, in the linear case, as a superposition of both limit cases. In this study the response to pressure excitation is investigated only.
For the derivation of the pressure excitation method a homogeneous mean flow and harmonic time dependence is assumed. From theoretical considerations, see [9,14], the fluctuating pressure field for the first transverse mode is given by

$$(1)\quad p'(x,r,\varphi,t) = \mathrm{Re}\left[P(x)\,\mathrm{J}_1\left(\frac{2\,r\,s_{10}}{d_{cc}}\right)\,\cos(\varphi)\,e^{i(\omega t-\pi/2)}\right]$$

where

$$(2)\quad P(x) = \bar{\rho} c\,\hat{g}\left[R_{FP}\,e^{-k^{+}x} + e^{-k^{-}x}\right]$$

and

$$(3)\quad k^{\pm} = \frac{k}{1-M^2}\left(-M \pm \sqrt{1-\left(\frac{f_{cut}}{f}\right)^2}\right),$$

$$(4)\quad k = \frac{2\pi f}{c},\ f_{cut} = \frac{s_{10}\,c}{\pi\,d_{cc}}\sqrt{1-M^2}.$$

With the definition of the effective pressure amplitude $\hat{p}$ by

$$(5)\quad \hat{p} = 2\bar{\rho} c \hat{g} J_1\left(\frac{2\,r\,s_{10}}{d_{cc}}\right),$$

the fluctuating pressure in the domain is finally given by

$$(6)\quad p'(x,y,t) = \mathrm{Re}\left[\frac{\hat{p}}{2}\cos(k_y\,y)\left(R_{FP}\,e^{-k^{+}x} + e^{-k^{-}x}\right)e^{i(\omega t-\pi/2)}\right],$$

where the dependency on cirumferential direction φ has been transformed into an equivalent wave number

representation with a y-coordinate originating at the single flame center line, viz.

(7) $\varphi \rightarrow k_y\, y.$

The reflection coefficient of the face plate R_{FP} is difficult to obtain. For the purpose of the studies presented in this paper it is set to an acoustic energetically neutral form, viz.

(8) $R_{FP} = \frac{1-M}{1+M},$

The factor $\frac{f_{cut}}{f}$ in Eq. (3) addresses the effect of frequency f on the mode shape, as soon as the system is excited above the cut-on frequency f_{cut} of the first transverse mode, see Eq. (4). In this investigation this frequency dependency is neglected by setting the factor to unity,viz.

(9) $\frac{f_{cut}}{f} = 1.$

The pressure fluctuations in the domain are generated through a periodically fluctuating source and drain, respectively, of mass on the excitation boundaries, see Fig. 2 and Fig. 3, on top of periodic conditions for the primary variables. Furthermore, the system is set-up and solved for axis-symmetric conditions.
The fluctuating mass flux is given by

(10) $\frac{\dot{m}'}{A} = \bar{\rho}\, v_i' n_i,$

where n_i is the normal vector perpendicular to the boundary where the mass sources are imposed. On basis of the pressure fluctuations according to Eq. (6) the corresponding fluctuating velocity v_i' in Eq. (10) reads

(11) $v'(x,r,\varphi,t) = \mathrm{Re}\left[-\frac{\hat{p}}{2\bar{\rho}c} k_y \sin(k_y y)\, V(x) e^{i(\omega t - \pi/2)}\right],$

with

(12) $V(x) = \mu_+ R_{FP}\, e^{-ik^+ x} + \mu_- e^{-ik^- x}$

and

(13) $\mu_\pm = \frac{-i}{k - Mk^\pm}.$

Essentially, the effective pressure amplitude $\hat{p}$ serves as user-input and controls the imposed pressure amplitude in the domain.

2.2. Turbulence and combustion modelling

Favre-averaged Navier-Stokes equations are used to describe the thermofluiddynamics of the system. Special attention is paid to the averaged momentum conservation equation, which is given by

(14) $\frac{\partial v_i}{\partial t} + u_j \frac{\partial v_i}{\partial x_j} = -\frac{1}{\rho}\frac{\partial p}{\partial x_i} + \frac{1}{\rho}\frac{\partial}{\partial x_j}\left(\tau_{ij} - \rho\widetilde{v_i''v_j''}\right) + S_M,$

where Einstein summation is used. The quantity τ_{ij} denotes the molecular stress tensor and S_M a momentum source term. Through averaging the unresolved Reynolds stress tensor

(15) $\mathrm{Re}_{ij} = \rho\widetilde{v_i''v_j''}$

occurs, where $\tilde{\blacksquare}$ denotes the averaging operator for undetermined, turbulent fluctuations. By assuming scale separation of turbulent and chemical time scales, it is known for simple shear flow that the $k-\epsilon$ turbulence model, based on the eddy cascade hypothesis, is appropriate to provide closure by

(16) $-\rho\widetilde{v_i''v_j''} = \rho\nu_t\left(\frac{\partial v_i}{\partial x_j} + \frac{\partial v_j}{\partial x_i} - \frac{2}{3}\frac{\partial v_k}{\partial x_k}\delta_{ij}\right) - \frac{2}{3}\rho k\delta_{ij},$

where

(17) $k = \frac{1}{2}\widetilde{v_i''v_j''}$

is the Favre-averaged turbulent kinetic energy and ν_t the turbulent kinematic viscosity, which is modeled in terms of k and ε by

(18) $\nu_t = c_\mu \frac{k^2}{\varepsilon},$

with $c_\mu = 0.09$ [1] and the Favre-averaged turbulent dissipation ε. For the variables k and ε two additional transport equations are solved, viz. [1]

(19) $\frac{\partial(\rho k)}{\partial t} + \frac{\partial}{\partial x_j}(\rho v_j k) = \frac{\partial}{\partial x_j}\left[\left(\mu + \frac{\mu_t}{\sigma_k}\right)\frac{\partial k}{\partial x_j}\right] + P_k - \rho\varepsilon,$

(20) $\frac{\partial(\rho\varepsilon)}{\partial t} + \frac{\partial}{\partial x_j}(\rho v_j \varepsilon) = \frac{\partial}{\partial x_j}\left[\left(\mu + \frac{\mu_t}{\sigma_\varepsilon}\right)\frac{\partial \varepsilon}{\partial x_j}\right] + \frac{\varepsilon}{k}(C_{\varepsilon 1}P_k - C_{\varepsilon 2}\rho\varepsilon),$

with

(21) $P_k = \mu_t\left(\frac{\partial v_i}{\partial x_j} + \frac{\partial v_j}{\partial x_i}\right)\frac{\partial v_i}{\partial x_j} - \frac{2}{3}\frac{\partial u_k}{\partial x_k}\left(3\mu_t\frac{\partial u_k}{\partial x_k} + \rho k\right),$

where $\sigma_k, \sigma_\varepsilon, C_{\varepsilon 1}$ and $C_{\varepsilon 2}$ denotes model constants.
Taking the curl of the averaged momentum Eq. (14) yields the vorticity conservation equation, viz.

(22) $\frac{\partial \Omega_i}{\partial t} + u_j\frac{\partial \Omega_i}{\partial x_j} = \Omega_j\frac{\partial u_i}{\partial x_j} - \Omega_i\frac{\partial u_j}{\partial x_j} + \frac{\varepsilon_{ijk}}{\rho^2}\frac{\partial \rho}{\partial x_j}\frac{\partial p}{\partial x_k} + \mathrm{rot}\left[\frac{1}{\rho}\frac{\partial}{\partial x_j}\left(\tau_{ij} - \rho\widetilde{v_i''v_j''}\right)\right] + \mathrm{rot}[S_m],$

where Ω_i denote the i-th component of the vorticity vector, ε_{ijk} the Levi-Civita symbol and rot the unevaluated rotation operator. Besides stretching or tilting of vorticity due to velocity gradients and compressibility as well as diffusion of vorticity due to the viscous effects, Eq. (22) captures the change of vorticity due to baroclinic effects through the term

(23) $\frac{\partial \Omega_B}{\partial t} = \frac{\varepsilon_{ijk}}{\rho^2}\frac{\partial \rho}{\partial x_j}\frac{\partial p}{\partial x_k},$

which is active in situations where pressure and density gradients are misaligned. Baroclinic effects directly influence the velocity fields and therefore turbulent kinetic energy and dissipation rate, see Eq. (19) and (20). The baroclinic production of vorticity plays an important role in the following investigations of the flame dynamics.
A global, single-step reaction is used to account for the combustion process, viz.

(24) $2H_2 + O_2 \rightarrow 2H_2O.$
Dissociation of H_2O in form of a backward reaction is not

considered, leading to overpredicted combustion temperatures. For the investigation of flame dynamics, however, that influence should be rather low.
A “mixed is burnt” approach is used for the non-premixed combustion modeling, where the time scales of chemical reaction are assumed sufficiently smaller than of the propellant mixing. The reacting rate limiting mixing process, in turn, is controlled by turbulence. Consequently, the Eddy Dissipation Model (EDM) developed by [15] is applied. In the framework of the EDM the local heat release rate is calculated from the mean burning rate of the fuel (here $\mathrm{H_2}$), which is given by

$$(25)\ \overline{\rho\dot{\omega}_{\mathrm{H_2}}} = A\rho\frac{\varepsilon}{k}\min\left(Y_{\mathrm{H_2}}, \frac{Y_{\mathrm{O_2}}}{s}, B\frac{Y_{\mathrm{H_2O}}}{(1+s)}\right),$$

where the mass stoichiometric ratio s reads as

$$(26)\ s = \frac{\nu'_{\mathrm{O_2}} W_{\mathrm{O_2}}}{\nu'_{\mathrm{H_2}} W_{\mathrm{H_2}}}.$$

The turbulent time scale

$$(27)\ \tau = \frac{k}{\varepsilon}$$

controls the reaction rate and the influence of kinetics is excluded.

2.3. Real-gas treatment

In the injection region of the propellants in supercritical systems real gas behavior is crucial. The change of specific internal energy, specific enthalpy and specific entropy, accounting for real gas effects, are typically evaluated through integration from a given, tabulated reference state in terms of temperature, specific volume and pressure $(T_{ref}, v_{ref}, p_{ref})$ to a target state (T, v, p). As integration path, however, an intermediate step through an ideal gas regime is used. Thermodynamically, the overall integration can be described as a three step integration consisting of an initial isothermal change to a valid ideal gas state, an isochoric change within the ideal gas regime, and a final isothermal change to the target state, again. As ideal gas regime the limit case of zero pressure and infinite specific volume $(p \to 0, v \to \infty)$ to exclude intermolecular forces is used. Altogether the internal energy is given by

$$(28)\ u(T,v) = u\left(T_{ref}, v_{ref}\right) + \int_{v_{ref}}^{v=\infty}\left[T\left(\frac{dp}{dT}\right)_v - p\right]dv|_{T_{ref}} + \int_{T_{ref}}^{T} c_{v,ref}\,dT - \int_{v}^{v=\infty}\left[T\left(\frac{dp}{dT}\right)_v - p\right]dv|_T,$$

and the specific entropy by

$$(29)\ s(T,v) = s\left(T_{ref}, v_{ref}\right) + \int_{v_{ref}}^{v=\infty}\left(\frac{dp}{dT}\right)_v dv|_{T_{ref}} + \int_{T_{ref}}^{T}\frac{c_{p,ref}}{T}dT - R\ln\left(\frac{p}{p_{ref}}\right) + \int_{v}^{v=\infty}\left(\frac{dp}{dT}\right)_v dv|_T,$$

where the specific heat capacity at constant volume $c_{v,ref}$ and at constant pressure $c_{p,ref}$ at the reference state are evaluated from NASA polynoms, see [16].
The evaluation of Eq. (28) and Eq. (29) requires a cubic equation of state (EOS) to account for real gas effects. In the present work, the EOS according to Soave-Redlich-Kwong is used to couple pressure p, temperature T and molar volume v by

$$(30)\ p = \frac{RT}{v-b+c} - \frac{a(T)}{v(v+b)},$$

where the following quantities are used:

$$(31)\ b = 0.08664R\frac{T_c}{p_c},$$

$$(32)\ a(T) = a_0\,\alpha(T),$$

$$(33)\ \alpha(T) = \left(1+\kappa\left(1-\sqrt{\frac{T}{T_c}}\right)\right)^2, a_0 = 0.42747\,R^2\frac{T_c^2}{p_c},$$

$$(34)\ \kappa = 0.480 + 1.574\hat{\omega} - 0.176\hat{\omega}^2,$$

and $\hat{\omega}$ is the acentric factor. The quantities $\blacksquare_c$ denote the state at the critical point.
Further quantities can be derived from the internal energy. Specific enthalpy is given by

$$(35)\ h(T,v) = u(T,v) + pv,$$

specific heat capacity at constant volume c_v at the given state (T, v) is calculated by

$$(36)\ c_v(T,v) = T\left(\frac{\partial u}{\partial T}\right)_v,$$

and the specific heat capacity at constant pressure c_p is then evaluated by

$$(37)\ c_p(T,v) = c_v(T,v) - T\left(\frac{\partial p}{\partial T}\right)_v^2\left(-\frac{\partial p}{\partial v}\right)_T^{-1}.$$

The significant impact of real gas behavior on the thermodynamic states and fluid properties can be studied e.g. in [17].
In the present work oxygen is treated as real gas, whereas the fuel hydrogen is treated as ideal gas in the entire domain.

2.4. Numerical setup

Single flame configurations allow for a substantial reduction of the computational domain. For the pressure excitation rotational symmetric conditions are valid, hence further reduction to only a two dimensional setup using symmetry boundary condition is possible.
The computational domain is shown in Fig. 3. Axis symmetric conditions are used at the flanges. At the top boundary a free slip wall to ensure periodicity is applied together with a mass source term according to Eq. (10). The described pressure fluctuations are also prescribed at the outlet to ensure consistent conditions. The nozzle, however, is not included to guarantee a resonance free system. In the vicinity of the injection the face plate is described as a no-slip wall. At the inlet of the recess the mass flows as well as the injection temperatures of oxygen and hydrogen are prescribed.
The considered chamber volume is set to 1/42 of the entire chamber volume. The corresponding area ratio between the recess and the virtual chamber volume is given by $\mathrm{A_r} = 0.133$.
The field equations are discretized on a qadrilateral mesh, see Fig. 4. The spatial resolution is increased in the propellant mixing and reaction layer. To keep computational efforts within reasonable limits the grid size is stretched in radial and axial direction.

Altogether the system is discretized on 47 000 grid cells and solved on a four core standard workstation.
For the simulations the commercial solver ANSYS-CFX 14.0 is used. In a first step a steady state result for a specific load point is computed using RANS equations setting the effective pressure amplitude to zero. In a second step, unsteady RANS computations with a time step of $\Delta t = 2e\text{-}6s$ are conducted and the flame response is studied under acoustic excitation.

3. TEST CASE CONFIGURATIONS

In this section the test case for the flame response studies is presented including the geometry and the considered load points. Moreover, the system in analyzed in terms of dominant acoustic frequencies.

3.1. BKD test chamber

The combustion chamber D (in German Brennkammer D) operated at the Institute of Space Propulsion of the German Space Agency (DLR) Lampoldshausen is a fully equipped representative rocket engine in a downscaled configuration, which operates at typical upper stage engine conditions (thrust level of 25 kN; chamber pressure of 70-80 bar). The BKD cylindrical combustion chamber (diameter: 80 mm, length: 210 mm), the feed and injection system and the nozzle are shown in Fig. 5. The injection system comprises 42 H_2/O_2 coaxial injectors. The thermodynamic condition of O_2 at the injection are of particular interest in this test case because of its supercritical pressure state but subcritical temperature state, see [11]. Supercritical propellants are advantageous for the intended studies, since the coupling of the acoustic fields with the combustion process can be investigated without the influence of atomization and vaporization. Thermoacoustic instabilities with acoustic pressure amplitudes up to 10 bar for the first transverse mode have been experimentally observed in [12,18].
Two load points are considered in the numerical simulations. The operative conditions in terms of mass flow rate $\dot{m}_{H_2/O_2}$, injection temperatures T_{H_2/O_2} and dome pressures p_{H_2/O_2} are reported in Tab. 1.

	LP3	**LP4**
$\dot{m}_{H_2}\ [\mathrm{kg}/s]$	0.96	0.96
$\dot{m}_{O_2}\ [\mathrm{kg}/s]$	5.77	5.75
$ROF[-]$	6	6
$T_{H_2}\ [K]$	47.62	95.66
$T_{O_2}\ [K]$	107.68	111.42
$p_{H_2}\ [bar]$	90.12	102.92
$p_{O_2}\ [bar]$	91.89	94.10
$p_{cc}\ [bar]$	80.22	80.04

TABLE 1: Experimental data for two load points (LP), see **[11]**, and estimated chamber pressure.

The chamber pressure p_{cc} is derived from chemical equilibrium conditions. For choked throat conditions in the nozzle, the mass flow rate must fulfill the gas dynamic relation

(38) $\dot{m} = \frac{\Gamma p_{cc} A_t}{\sqrt{R T_{cc}}}$,

where $\mathrm{T_{cc}}$ denotes the chamber temperature, R the gas constant, $\mathrm{A_t}$ the throat area and Γ a function of the specific heat ratio γ, see [19]. The chamber pressure p_{cc} is iteratively varied and used to calculate $\mathrm{T_{cc}}$, Γ and R by evaluating the CEA software, see [20,21], until the properties of the combustion products are such that the throat mass flow, given by Eq. (38), matches the injected mass flow rate. The estimated chamber pressures are also reported in Tab. 1.

3.2. Eigenfrequency analysis

In order to apply the excitation method to a single flame configuration the cut-on frequency of the first transverse mode and the relevant frequency range to consider has to be known. For that purpose, eigenfrequency analyses are used. For the eigenfrequency analysis a mean flow field comprising only hot combustion products is included. Such conditions are essential to gain meaningful eigenfrequencies for the first transverse mode. For further details about the numerical setup it is referred to [22,23].
The mode shape of the first transverse mode in terms of pressure amplitude distribution is shown in Fig. 7. The transverse orientation can be seen at the inlet. The axial dependence of the model shape showing longitudinal character in the chamber is clearly visible.
The determined mode frequencies of LP3 and LP4 are reported in Tab. 2 showing only a weak dependence on load point conditions. In general, the mode frequency for the first transverse mode is given by about 11 600 Hz.

	LP3	LP4
$\mathrm{f_{T1}}\ [\mathrm{Hz}]$	11 626	11 624

TABLE 2: Determined mode frequencies for LP3 and LP4 for the first transverse mode.

4. FLAME DYNAMIC ANALYSIS

In this section the analyses of the flame dynamics are presented. First, a feasibility analysis of the reduction from 3D to 2D computations is shown and the mean state of the single flame domain is illustrated. Afterwards the dynamic response of the flame to pressure excitation is presented and analyzed in detail. Finally, flame transfer functions are derived and their driving potential for thermoacoustic feedback is highlighted.

4.1. Validation of 3D to 2D reduction

A single flame configuration states geometrically an axis-symmetric system. The coaxial injection does not provide swirl in circumferential direction. Nevertheless, the 3D simulation results do not necessarily have to be axis-symmetric. To validate the reduction a comparison between the 2D temperature field and the corresponding 3D results for the steady-state case without acoustic excitation is shown in Fig. 8. The temperature field distributions as well as its maximum values are in very good agreement. The reduction of grid cells from about 8.2 million to only 47 000 is enormous.

4.2. Steady fields

The steady state field results for LP3 and LP4 in terms of volumetric heat release rate $\dot{q}$, density ρ and mass fraction

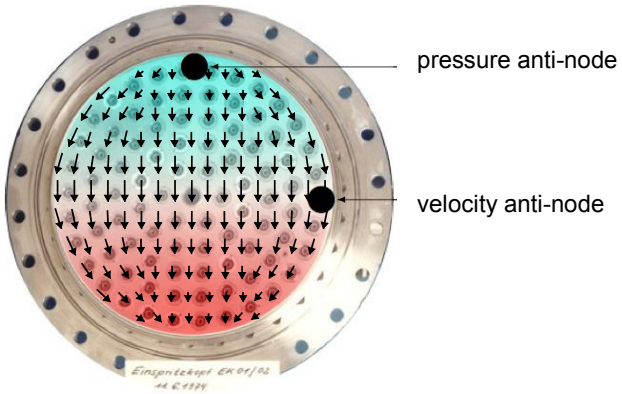

FIGURE 1: Typical face plate injector pattern, overlayed pressure amplitude distribution (colored) and corresponding acoustic velocity field (arrows).

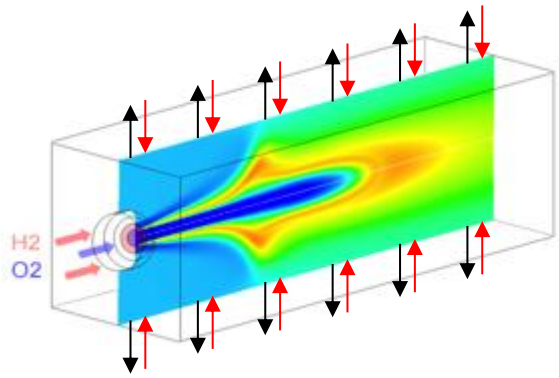

FIGURE 2: Single flame configuration (temperature field) and illustrated excitation method (arrows).

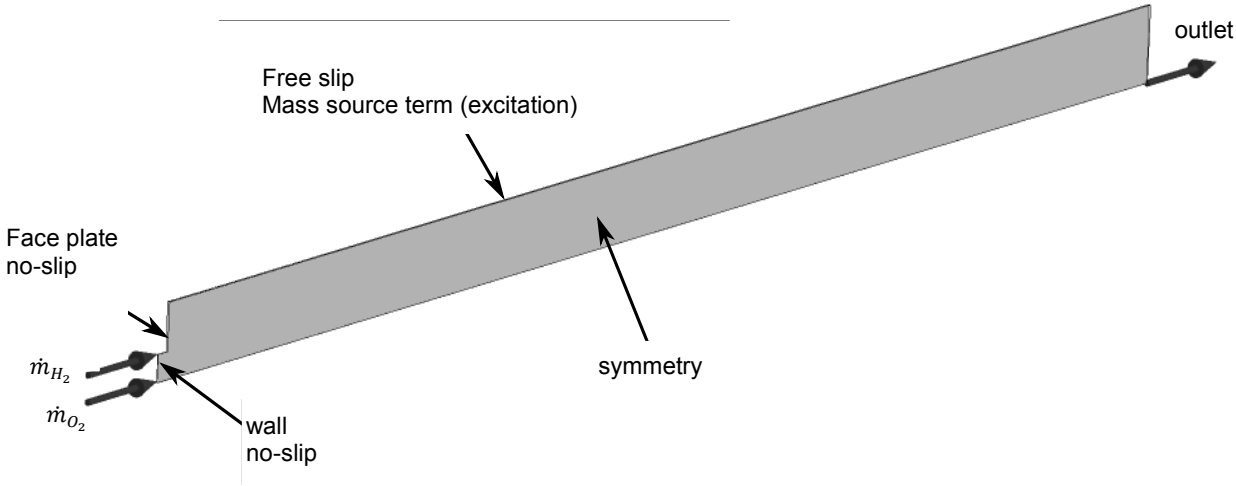

FIGURE 3: Numerical setup of the computed axis-symmetric single flame configuration.

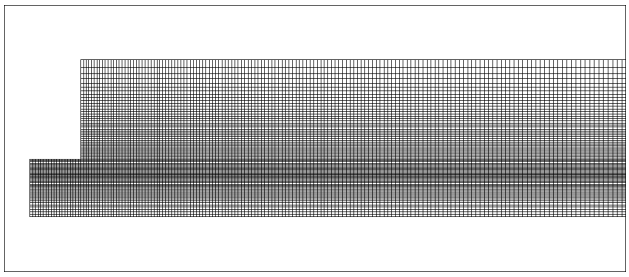

FIGURE 4: Computational mesh in the vicinity of injection.

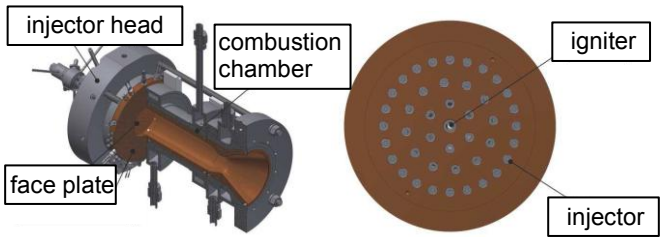

FIGURE 5: Left: DLR's BKD combustion chamber configuration. Right: BKD injectior pattern, see [11].

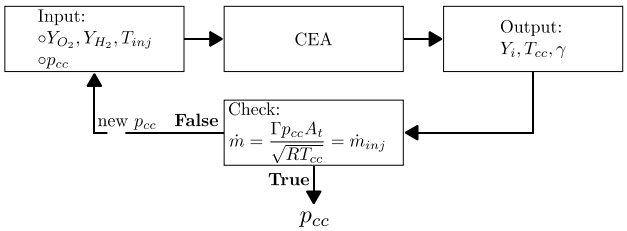

FIGURE 6: Iterative procedure to evaluate chamber pressure for the given experimental data.

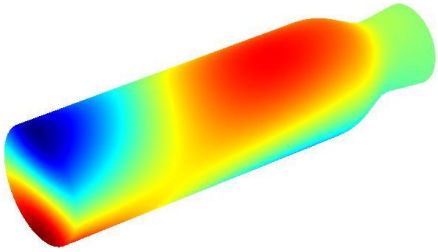

FIGURE 7: Mode shape in terms of pressure amplitude distribution of the first transverse mode (T1).

of oxygen Y_{O_2} are shown in Fig. 9. In general, a considerable longer flame length in case of LP3 is observed in each quantity.
From the distribution of the volumetric heat release rate two regions can be distinguished. Between the inlet and an axial position of approximately 15 mm, locally high values occur and the influence of a recirculation bubble is present. Further downstream the heat release rate is distributed more uniformly.
In the density fields the influence of the real gas is especially obvious. Strong density gradients in radial direction with a maximum density ratio between O_2 and H_2 of approximately 300 dominate the first third of the chamber length.
Chemical reactions take place in areas were H_2 and O_2 are mixed on a molecular level, which are located in the shear layer, described by the green zone of the O_2-mass fraction field (bottom) in Fig. 9.

4.3. Flame dynamic analysis

In the next step, the single flame configurations are subjected to acoustic pressure excitation. In this investigation the effective pressure amplitude is restricted to 3% of the mean pressure, which corresponds to an amplitude of approximately 2.4 bar.
Detailed studies of possible coupling mechanism are conducted for the operating conditions of LP3 and an excitation frequency of 11 000 Hz. Afterwards, a frequency band around the determined mode frequencies, see Tab 2, is considered.

4.3.1. Spatial differentiation of coupling

The field of fluctuating heat release as consequence of the pressure excitation in shown in Fig. 10 (middle) in form of a Dynamic Mode Decomposition. The DMD method decomposes the input time series into orthogonal modes with respect to the correlating frequency, which allows for the investigation of the most energetic field structures at the frequency of excitation, see e.g. [24]. For a detailed mathematical description of the DMD method it is referred to [25]. The DMD results are presented in form of an amplitude weighted phase plot. The color indicates the relative phase with respect to an arbitrarily chosen reference phase and the amplitude is described by the color's intensity, whereby white depicts zero amplitude.
The DMD results are plotted together with the field of the heat release rate $\dot{q}$ (top) and the temperature field (bottom). Especially the phase information in the DMD results indicates different behavior of the flame dynamics in regions close to the injector and in the remaining region further downstream.
To gain better insight in those regions corresponding near and far zones are defined, see Fig. 10. The near zone reaches from the inlet to 15mm further downstream, whereas the far zone comprises the remaining region. In the following these zones are investigated in more detail.

4.3.2. Near zone

The DMD structure in the near zone is shown in more detail in Fig. 11. A prominent continuous phase change can be observed. It can be shown, that the change of phase corresponds to the velocity of the flow. Such a phase distribution typically indicates a convective transport phenomenon.
Fig. 12 shows the most energetic structures of the velocity fluctuations in axial direction, which are triggered at the H_2-inlet due to a fluctuating density ρ'_{H_2} according to mass conservation by

$$\bar{v}_{H_2} + v'_{H_2} = \frac{\dot{m}_{H_2}}{(\bar{\rho}_{H_2} + \rho'_{H_2})\, A_{H_2}}, \tag{39}$$

where A_{H_2} denotes the corresponding inlet area. The mass flow of hydrogen $\dot{m}_{H_2}$ is constant by definition at the boundary. The fluctuations of density, in turn, are caused by the pressure fluctuations p' at the inlet. The periodically triggered velocity fluctuations at the H_2-inlet are transported convectively downstream, depicted by a continuous phase-change in direction of flow, which is described by the upper continuous transition of color from red to turquoise in Fig. 12. In contrast, at the O_2-inlet velocity fluctuation of significant amplitude do not occur.
In the shear layer of H_2 and O_2, a periodically fluctuating axial velocity occurs as well, but with a different phase (blue/purple) compared to the triggered fluctuations at the H_2-Inlet (red). These fluctuations are also convectively transported downstream.
Based on the observations, different coupling mechanisms are derived in the near zone. Kelvin-Helmholtz instabilities lead to periodic vortex shedding in the shear layer between H_2 and O_2. Those vortical fluctuations get convected downstream, causing an increase of turbulent mixing at each location, which, in turn, periodically increases the chemical reaction rate. Furthermore, periodic wrinkling of the flame sheet enlarges the surface and thus also leads to fluctuations of the heat release rate, which was observed experimentally in [26]. Finally, velocity fluctuations lead to fluctuating mass flow rates within the domain, which can modulate the burning rate and therefore amplify the fluctuating heat release rate.

4.3.3. Far zone

The mode of heat release rate fluctuations in the far zone is presented in Fig. 10. For a better visibility of the heat release rate fluctuations with a less significant magnitude in the far zone, a saturation level was chosen and depicted by black color. By comparing the heat release modes, it can be seen most significantly that the phase change of the heat release fluctuations in the far zone occur at a different length scale than in the near zone. Furthermore, the length scale of axial velocity fluctuations, shown in Fig. 13, clearly correlates to those of the heat release rate in Fig. 10, and thereby confirms the occurrence of different structures in the far zone. Due to comparable axial flow velocities in near and far zone, a convective transport of vortices in the far zone can be ruled out. The coupling mechanism in the far zone generates velocity fluctuations in a wide range, leading to a fluctuating heat release rate, which is almost completely in-phase throughout a broad area. Additionally, the mode of the acoustic pressure fluctuations in the entire domain is considered in Fig. 14 for different frequencies at an instant in time. The length scale of the phase change correlates also to those of the heat release rate fluctuations and the axial velocity fluctuations in the far zone, see Fig. 10 and Fig. 13, which indicates a direct correlation between acoustic pressure fluctuations and heat release fluctuations.
Due to Mach-number effects and boundary conditions axial acoustic pressure gradients occur in the domain with a frequency dependent location of maximum pressure amplitude, see Fig. 14. At the same time strong density

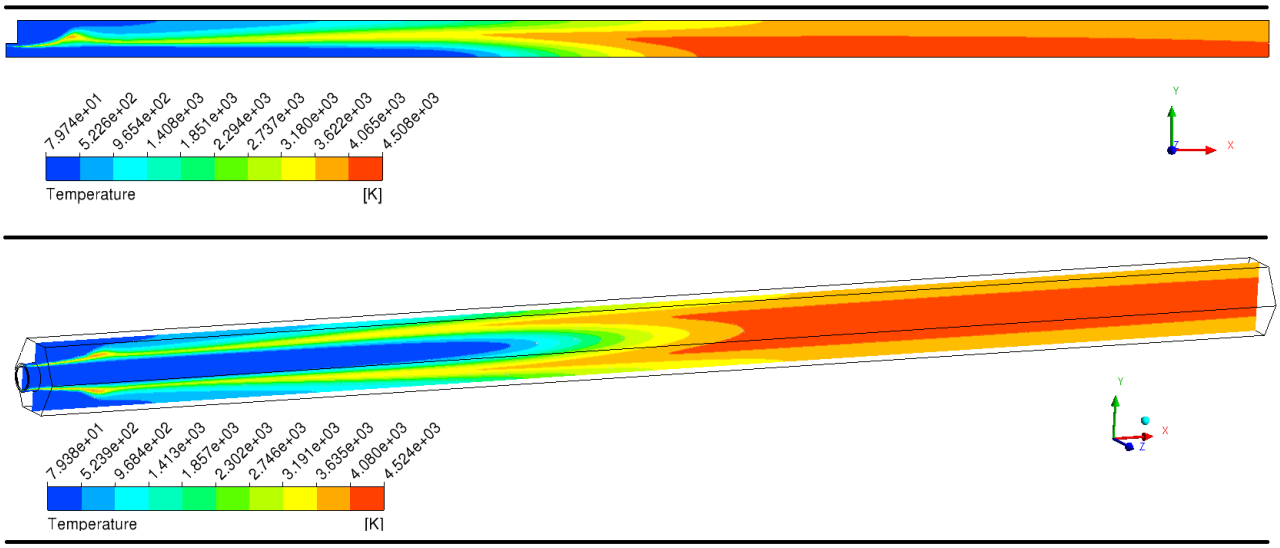

FIGURE 8: Resulting temperature field of the simulation with the quasi 2D-domain (top), discretized with 47 000 grid cells, compared to the temperature field of the simulation with the 3D-domain and 8 million grid cells.

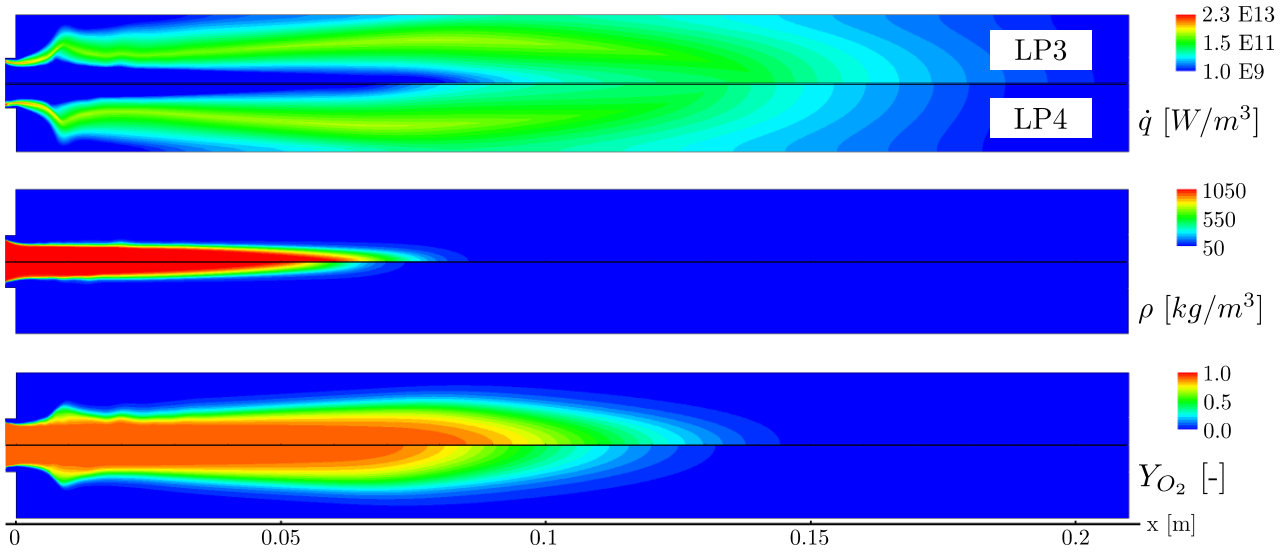

FIGURE 9: Comparison of steady state field results for LP3 and LP4 in terms of volumetric heat release rate $\dot{q}$ (top), density ρ (middle) and mass fraction of Y_{O_2} oxygen (bottom).

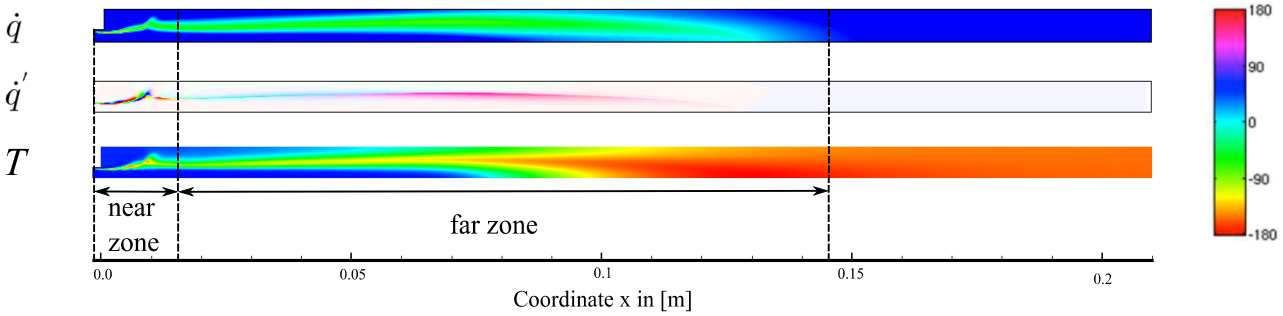

FIGURE 10: Volumentric heat release for LP3 (top), fluctuating heat release rate (middle) and temperature field (bottom) as well as discrimination of a near and far zone. Steady state heat release scale, see Fig. 9. Temperature scale, see Fig. 8.

gradients between O_2 and H_2 in radial direction are misaligned to those acoustic pressure gradients, see Fig. 9, triggering the baroclinic production of vorticity according to Eq. (23). Consequently, those vortices periodically increase mixing and thus the chemical reaction rate, leading to periodic heat release rate fluctuations of significant amplitude. In the simulations, the baroclinic effects are captured through a modulation of turbulent kinetic energy and dissipation rate, see Eq. (19) and (20) and therefore influence the burning rate in the EDM, see Eq. (25).

A larger zone of mixing and hence a wider region of emerging density-gradients leads to a stronger vorticity production in a volume-integrated point of view. Therefore, the larger flame length in case of LP3 might lead to stronger baroclinic effects and in consequence to higher amplitudes of fluctuating heat release rate.

The mode of the vorticity fluctuations is shown in Fig. 15. As already discussed, vorticity fluctuations occur close to the injection, caused supposedly by periodic vortex shedding within the shear layer. In areas with density gradients, the baroclinic production of vorticity is clearly visible. The phase-change of the vorticity fluctuation mode in the near and far zone, with the frequency equal to the excitation frequency, correlates to the phase-change of the velocity fluctuations in axial direction, shown in Fig. 13 and consequently to the heat release mode, which is clearly depicted in Fig. 15.

In addition, the transient evolution of the turbulent kinetic energy in the near and far zone for one acoustic period is shown in Fig. 16. Two characteristic areas in the field of the turbulent kinetic energy can be observed. On the one hand, one characteristic region close to the injector within the shear layer is observed and at the end of the recess, caused by local vortex shedding at the edge. On the other hand, a significantly periodically varying turbulent kinetic energy is observed further downstream. The phenomenon of vorticity production due to misaligned pressure and density gradients is also experimentally observed in [26], which is called baroclinic vorticity driven instabilities.

4.4. Frequency dependency

In this section the dependency of the dynamic flame response to acoustic excitation on frequency is studied. At first, the modes of the heat release rate fluctuations, again with the frequency equal to excitation frequency, are compared in Fig. 17 at different excitation frequencies. For all frequencies, the modes of the heat release fluctuations are similar. Close to the injector, the convective structure can be observed for each mode. In the far zone, the phase-change of the heat release fluctuations occur at a different length scale, with respect to the continuous phase-change in the near zone, as it was discussed before.

For further analysis, the amplitude of the volume-integrated heat release rate fluctuations within the domain-volume [-2mm − 15mm] (near zone) is compared to the amplitude of the volume-integrated heat release rate fluctuations within the domain-volume [15mm − 210mm] (far zone) in Fig. 18 at different excitation frequencies. From a volume-integrated point-of-view it can be observed, that most of the heat release rate fluctuations occur in the far zone (ratio of 8-10), despite the fact that heat release fluctuations have dominating intensities within the near zone for all considered frequencies, as it is shown in Fig. 17. Nevertheless, the region of heat release is very thin compared to the far zone. This can also be illustrated by considering the mass fraction of O_2 in Fig. 9, where the "mixing zone" with spatial density-gradients and thus the area where heat release fluctuation occurs, ranges over a volume of significantly larger size compared to the near zone.

In Fig. 19 the volume-integrated heat release rate amplitude for the near zone is compared to the axial velocity amplitudes at the H_2-inlet for different frequencies. A direct correlation between the amplitude of the axial velocity and the amplitude of the volume-integrated heat release rate fluctuations is observed. Therefore, H_2-velocity fluctuations of bigger amplitude evoke greater mass flow rate fluctuations, which consequently lead to heat release fluctuations of larger amplitude. H_2-velocity fluctuations of bigger amplitude might also increase the perturbation of the shear layer, triggering additional shear layer instabilities.

As it was derived before, an increase in amplitude of the velocity fluctuations at the H2-inlet is evoked by an increased pressure amplitude. This is illustrated by comparing the amplitude of the pressure fluctuations at the inlet in Fig. 20 to the H_2 velocity fluctuations and the heat release fluctuations in Fig. 19.

In the far zone, an increase of amplitude of the heat release fluctuations is induced by additional baroclinic vorticity production, which is, in turn, evoked by stronger acoustic spatial pressure gradients. On the one hand, the frequency-dependent amplitude distribution of the acoustically excited pressure field in axial direction of the single-injector, illustrated in Fig. 14, shows a decrease in the wavelength with rising frequency and thus increasing wave number. Consequently, the spatial gradients of the acoustic pressure fluctuations get stronger, what implies greater vorticity production in areas of mean spatial density gradients. On the other hand, the transient pressure amplitudes for different frequencies at the axial location of x = 0.09 m, see Fig. 21, show an increasing number of turning points with rising frequency due to decreasing acoustic periods. The effects of positive and negative pressure gradients cancel each other. Followingly, only the unbalanced region is relevant, which gets smaller with increasing frequency. Thus, it can be assumed that there is a trade-off between the intensity and the size of the relevant region of the vorticity production, leading to one or several optima of greatest heat release fluctuations over time and frequency.

4.5. Flame Transfer Functions

In the linear regime, the Flame Transfer Function (FTF) is defined by

$$FTF = \frac{\hat{\dot{q}}/\bar{\dot{q}}}{\hat{p}/\bar{p}},$$

and correlates the Fourier-transformed signals of volume-integrated fluctuating heat release over the entire domain $\hat{\dot{q}}$ and pressure $\hat{p}$. For convenience the FTF is presented in non-dimensional form.

Fig. 22 shows a comparison of the FTF in terms of amplitude and phase between LP3 and LP4 for a reference pressure recorded at an axial position of 100 mm, which has been chosen such that it is located in the region of strong baroclinic vorticity production. Therein, the general trend of amplitude and phase are equivalent. However, the amplitude of LP3 is higher than for LP4, while smaller phase values are observed for LP3,

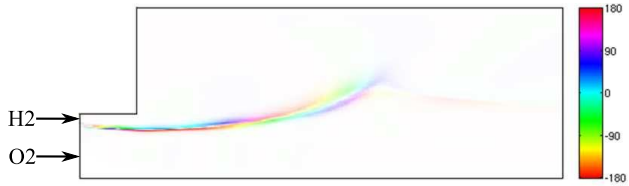

FIGURE 11: Mode of the heat release fluctuations in the near zone, with the frequency equal to excitation frequency at LP3 with 11000 Hz acoustic forcing.

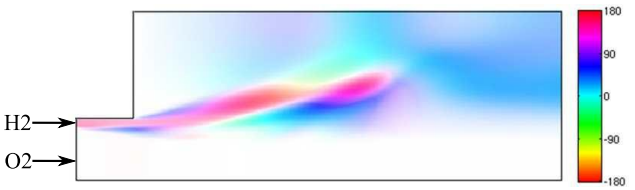

FIGURE 12: Mode of the axial-directed velocity fluctuations in the near zone, with the frequency equal to excitation frequency at LP3 with 11000 Hz acoustic forcing.

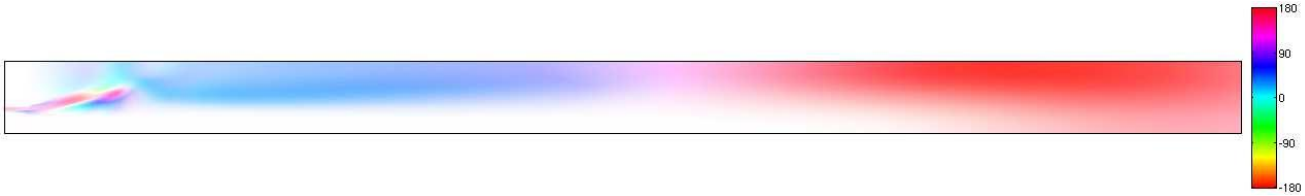

FIGURE 13: Mode of the axial-directed velocity fluctuations in the near and far zone, with the frequency equal to excitation frequency at LP3 with 11 000 Hz acoustic forcing.

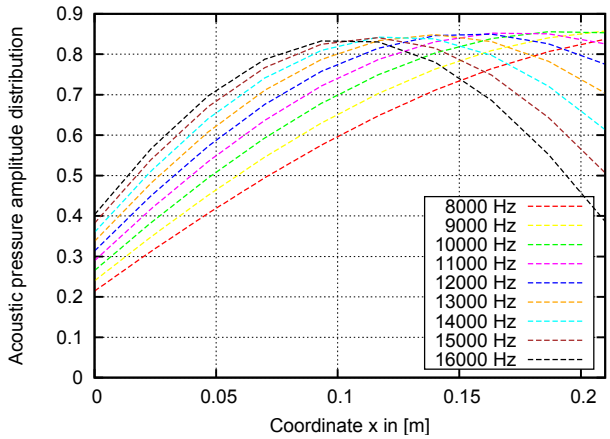

FIGURE 14: Frequency dependent axial pressure amplitude distribution at one instant in time (scaled with theoretically imposed pressure amplitude).

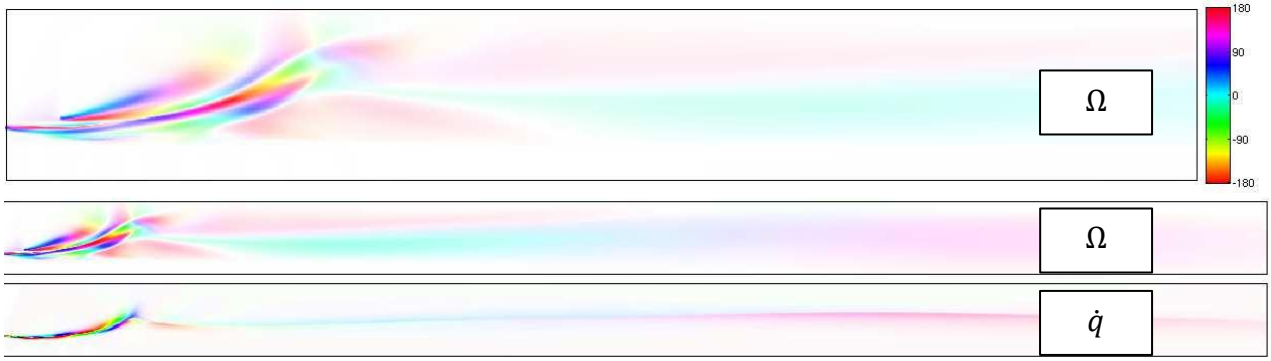

FIGURE 15: Mode of the vorticity fluctuations in the near and far zone (top/middle) compared to the mode of the heat release fluctuations, with the frequency equal to the excitation frequency at LP3 with 11 000 Hz acoustic forcing.

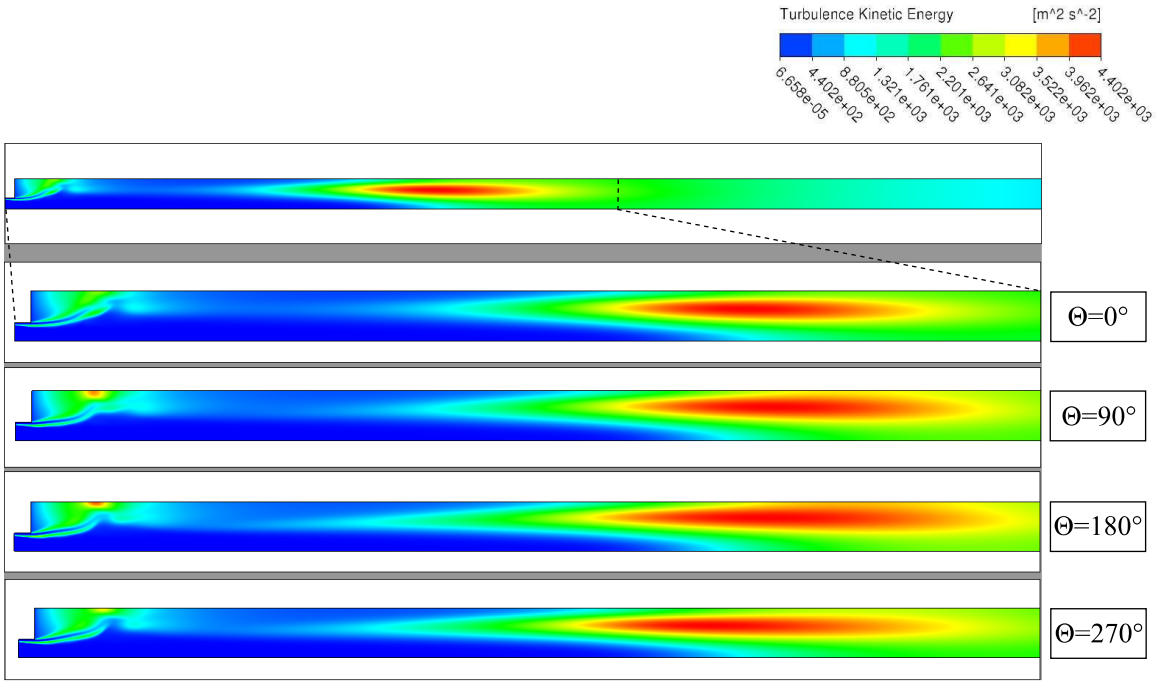

FIGURE 16: Periodic development of the turbulent kinetic energy in the near and far zone for one acoustic period at LP3 with 11 000 Hz acoustic forcing.

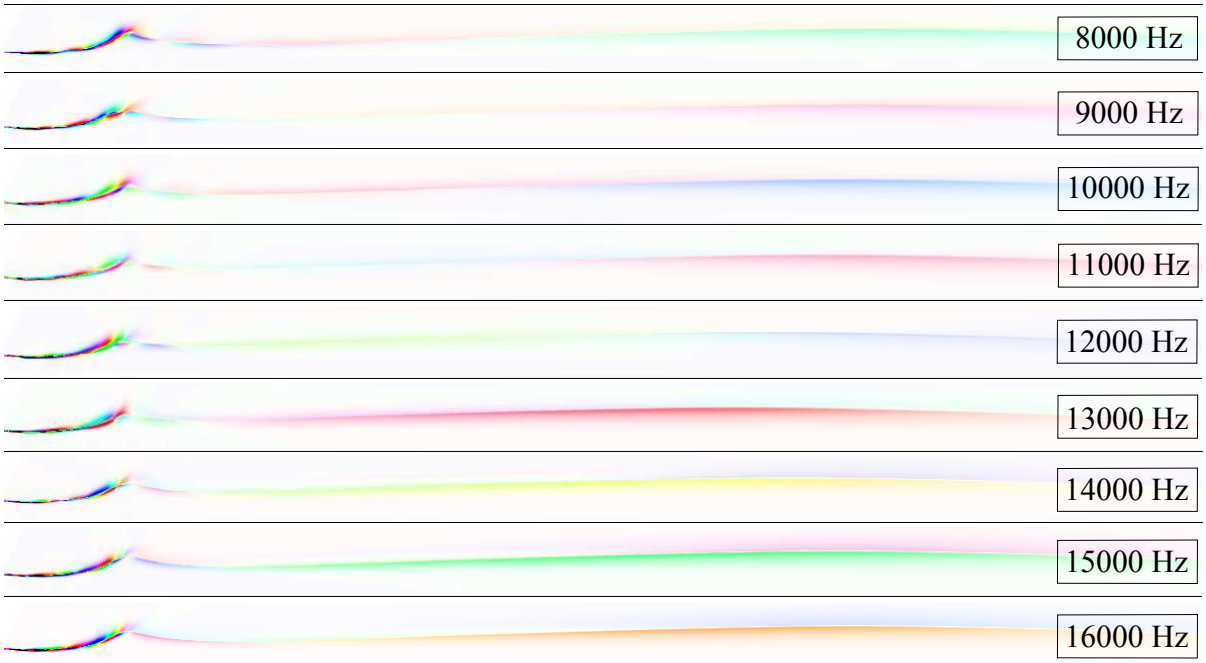

FIGURE 17: Modes of the heat release rate fluctuations in the near and far zone, each with the frequency equal to excitation frequency at LP3.

especially for lower frequencies. Consequently, a more intense coupling of the flame for LP3 is present.
The stronger coupling of LP3 can be emphasized by considering the response factor (RF), which is defined by

$$RF = \mathrm{Re}(FTF) = |FTF| \cos\big(\varphi(FTF)\big),$$

and indicates the coupling intensity of the acoustic and combustion. The smaller the phase, the stronger is the response of the flame at that amplitude. The RF is also shown in Fig. 22. Especially at the mode frequency, see Tab. 2, the RF of LP3 is significantly higher than for LP4. Preliminary studies on the thermoacoustic stability of the system using the calculated FTFs of this paper have been conducted in [7] and show indeed an instability for LP3.

5. CONCLUSION AND OUTLOOK

In the scope of presented work, URANS simulations were carried out to analyze the flame dynamics of DLR's experimental rocket combustion chamber BKD. A single flame configuration was subjected to acoustic pressure fluctuations according to the pressure distribution of the first transverse mode. Different frequencies were considered and the response of the H_2/O_2 turbulent combustion process under supercritical conditions was studied.
On basis of DMD results two zones were identified, where the field of the heat release rate fluctuations show distinguishing behavior. The occurring heat release fluctuations in each zone were traced back to two dominating coupling mechanisms. Both are induced by vorticity fluctuations, which are closely related to vortical velocity fluctuations and thus to fluctuations of the turbulent kinetic energy. In a near zone periodically fluctuating vorticity is generated by shear effects. In the far zone, the periodic baroclinic production of vorticity leads to fluctuating heat release rates. The applied EDM captures the influence of vorticity on the combustion. This zone-dependent behavior of the acoustically excited flame was observed in a representative band of frequencies.
Additionally the volume-integrated heat release fluctuations were determined in the near zone and in the far zone. Despite the fact that heat release rate fluctuations show locally high intensity close to the injector, in the volume-integrated sense, heat release fluctuations are signifcantly higher in the far zone by a factor of 8-10.
The amplitude and phase of the FTF for LP3 and LP4 were compared, showing that the response of the flame is more intense for LP3 than for LP4, which might be due to a larger flame length in case of LP3.
A profound analysis of the phenomena occurring in the near zone is not possible in detail, due to insufficient resolution of turbulent mechanisms in terms of the URANS simulation. Thus, Large-Eddy-Simulations (LES) are required for a better separation of the occurring phenomena. Moreover the influence of the O_2-injector on the dynamics of the system has to be analyzed. Another step in the analysis of the flame dynamics would also require a more profound combustion model to study the effects of kinetics.
So far, single flame configurations were only excited in terms of pressure. However, the influence of transverse velocity fluctuations on the heat release rate is of great interest.
Finally, the dependence of the flame response on amplitude needs to be investigated in order to account for saturation effects.

6. Acknowledgements

Financial support has been provided by the German Research Foundation (Deutsche Forschungs-gemeinschaft) in the framework of the Sonderforschungs-bereich Transregio 40.

7. Bibliography

[1] ANSYS, Ansys-CFX solver modeling guide.

[2] F. Culick and V. Yang, "Overview of Combustion Instabilities in Liquid-Propellant Rocket Engines," in American Institute of Aeronautics and Astronautics.

[3] J.C. Melcher and R.L. Morehead, "Combustion Stability Charac- teristics of the Project Morpheus Liquid Oxygen / Liquid Methane Main Engine," in 50th AIAA/ASME/SAE/ASEE Joint Propulsion Conference, DOI:10.2514/6.2014-3681, Cleveland, Ohio, USA, 2014.

[4] J. Pieringer, Simulation selbsterregter Verbrennungsschwingungen in Raketenschubkammern im Zeitbereich, 2008, Technical University of Munich, Ph.D. thesis.

[5] M. Schulze, M. Schmid, D. Morgenweck, S. Köglmeier, and T. Sattelmayer, "A Conceptional Approach for the Prediction of Thermoacoustic Stability in Rocket Engines," in 49th AIAA/ASME/SAE/ASEE Joint Propulsion Conference,doi:10.2514/6.2013-3779, San Jose, California, USA, 2013.

[6] D. Morgenweck, Modellierung des Transferverhaltens im Zeitbereich zur Beschreibung komplexer Randbedingungen in Raketenschubkammern, 2013, Technical University of Munich, Ph.D. thesis.

[7] M. Schulze, A. Urbano, M. Zahn, T. Sattelmayer, and M. Oschwald, "Thermoacoustic Feedback Analysis of a Cylindrical Combustion Chamber under Supercritical Conditions, doi:10.2514/6.2014-3776," in 50th AIAA/ASME/SAE/ASEE Joint Propulsion Conference, Cleveland, Ohio, USA, 2014.

[8] M. Schmid and T. Sattelmayer, "Influence of pressure and velocity perturbations on the heat release fluctuations for coaxial GH2/GO2 injection," in 4th European Conference for Aeronautics and Space Sciences, St. Petersburg, Russia, 2011.

[9] M. Schmid, Thermoakustische Kopplungsmechanismen in Flüssigkeitsraketentriebwerken, 2014, Technical University of Munich, Ph.D. thesis.

[10] T. Ramcke, M. Schmid, and T. Sattelmayer, "Response Characterization of a LOX-GH2 Flame to Forced Acoustic Pressure Fluctuations," in 5th European Conference for Aeronautics and Space Sciences, Munich, Germany.

[11] S. Gröning, "Test Case HF-7: LOX/H2-Combustion with self-sustained acoustic excitation," in 3rd REST Workshop on Combustion Instability Modeling, Vernon, France, 2014.

[12] S. Gröning, D. Suslov, M. Oschwald, and T. Sattelmayer, "Stability behaviour of a cylindrical rocket engine combustion chamber operated with liquid hydrogen and liquid oxygen," , Munich, Germany, 2013.

[13] D. Morgenweck, T. Sattelmayer, F. Fassl, and R. Kaess, "Influence of Scaling Rules on Loss of Acoustic Energy," Journal of Spacecraft and Rockets, vol. 48, no. 3, pp. 498-506, 2011.

[14] R. Kathan, Verlustmechanismen in Raketenbrennkammern, 2013, Technical University of Munich, Ph.D. thesis.

[15] B.F. Magnussen and B.H. Hjertager, "On Mathematical Modeling of Turbulent Combustion with Special Emphasis on Soot Formation and Combustion," in 16th Symp (Int) on Combustion, 1976.

[16] A. Burcat and B. McBride, "Ideal gas thermodynamic data for com- bustion and air-pollution use," in Technical Report TAE 697, 1993.

[17] S. Pohl, M. Jarczyk, M. Pfitzner, and B. Rogg, "Real gas CFD simulations of hydrogen/oxygen supercritical combustion," Progress in Propulsion Physics 4, pp. 583-614, 2013.

[18] S. Gröning and M. Oschwald, HF-7 test case: Synthesis, 2014, 3rd REST Workshop on Combustion Instability Modeling.

[19] G.P. Sutton and O. Biblarz, Rocket Propulsion Elements, 7th edition, Ed.: John Wiley and Sons, 2001.

[20] B.J. McBride and S. Gordon, Computer Program for Calculation of Complex Chemical Equilibrium Compositions and Applications, National Aeronautics and Space Administration, Lewis Research Center, Cleveland, Ohio 44135-3191, October 1994, Reference Publication, NASA RP-1311.

[21] GLENN RESEARCH CENTER, Chemical Equilibrium with Applications, http://www.grc.nasa.gov/WWW/CEAWeb/.

[22] M. Schulze, M. Schmid, and T. Sattelmayer, Eigenvalue Analysis for the Prediction of Initial Growth Rates of a Thermoacoustic Instability – HF-7 Test Case, 2014, Proceedings of the 3rd REST Modelling Workshop, SNECMA, Vernon.

[23] M. Schulze and T. Sattelmayer, Time and Frequency Domain Descriptions of Thermoacoustics in Rocket Engines with Focus on Dome Coupling - A Comparison, 2014, Sonderforschungsbereich/Transregio 40 – Annual Report 2014.

[24] M. Wierman et al., Investigation on Thermoacoutic Feedback on a Representative Test Chamber Configuration, Proceedings of the DFG SFB TRR 40 Summer Programm 2014.

[25] P.J. Schmid, "Dynamic mode decomposition of numerical and experimental data," Journal of Fluid Mechanics, vol. 656, pp. 5-28, 2010.

[26] A. Ghosh, The role of density gradients in liquid rocket engine combustion instability, 2008.

[27] R. Keller, M. Lempke, and P. Gerlinger, The Influence of Discretization and Unsteadiness on the Simulation of Rocket Combustors, Sonderforschungsbereich/Transregio 40 – Annual Report 2014.

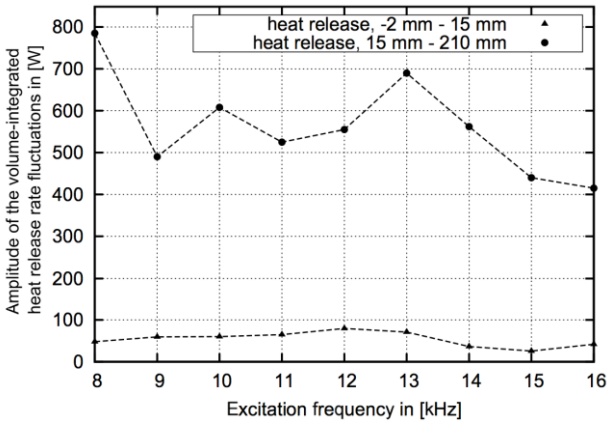

FIGURE 18: Comparing the amplitude of the volume-integrated heat release rate fluctuations, determined in near (-2 – 15mm) and far zone (15 – 210mm).

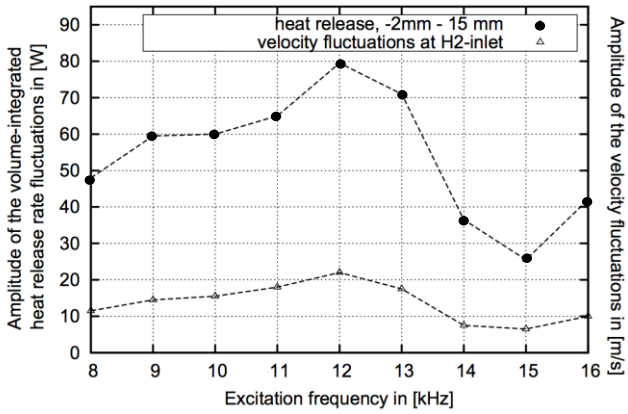

FIGURE 19: Comparing the amplitude of the volume-integrated heat release rate fluctuations, determined in the near zone (-2 – 15mm) to the amplitude of the axial velocity fluctuations at the H_2-inlet for different frequencies.

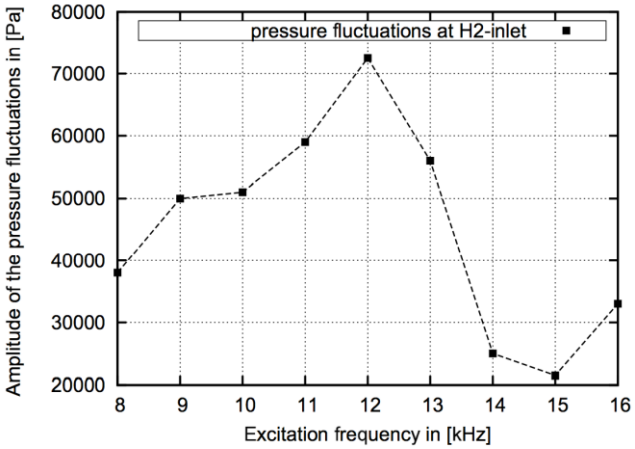

FIGURE 20: Amplitude of the pressure velocity fluctuations at the H_2-inlet for different excitation frequencies at LP3.

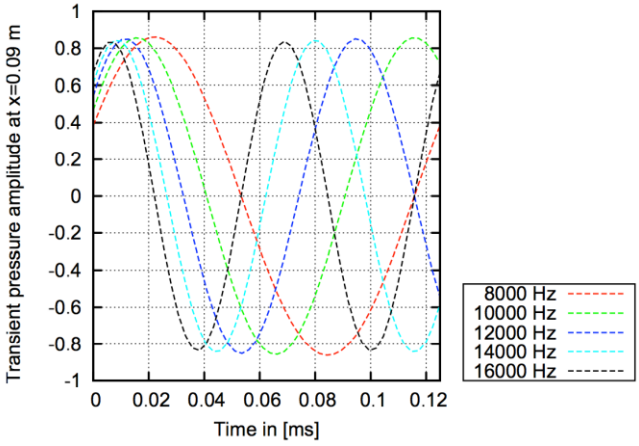

FIGURE 21: Transient acoustic pressure amplitude at the axial location of $x = 0.09$ m and conditions of LP 3.

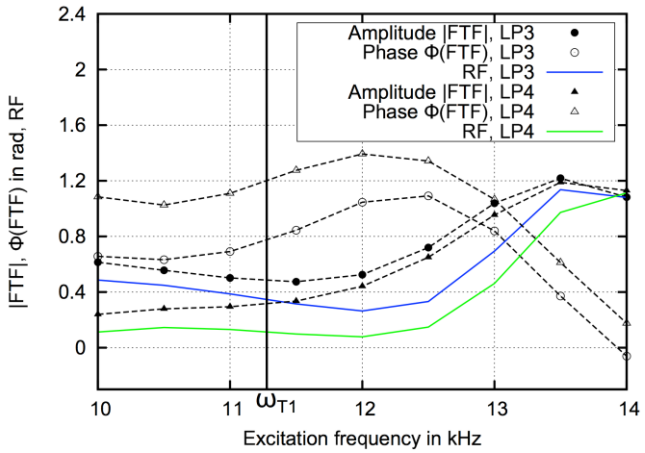

FIGURE 22: Comparison of the FTF for LP3 and LP4 for a frequency range between 10 000 and 14 000 Hz, with an interval of 500 Hz and a reference pressure at axial position of 100mm.